WPEDU-PR(18) 21539

A Stegmeir et al.

Global turbulence simulations of tokamak edge with GRILLIX

Preprint of Paper to be submitted for publication in Physics of Plasmas

This work has been carried out within the framework of the EUROfusion Consortium and has received funding from the Euratom research and training programme 2014-2018 under grant agreement No 633053. The views and opinions expressed herein do not necessarily reflect those of the European Commission.

Global turbulence simulations of the tokamak edge region with GRILLIX

A. Stegmeir[a], A. Ross[a], T. Body[a], M. Francisquez[b], W. Zholobenko[a], D. Coster[a], O. Maj[a], P. Manz[a], F. Jenko[a], B.N. Rogers[b], K.S. Kang[a]

[a]*Max-Planck-Institut für Plasmaphysik, D-85748 Garching, Germany*
[b]*Department of Physics and Astronomy, 6127 Wilder Laboratory, Dartmouth College, Hanover, NH 03755, USA*

Abstract

Turbulent dynamics in the scrape-off layer (SOL) of magnetic fusion devices is intermittent with large fluctuations in density and pressure. Therefore, the use of a global model is required that allows perturbations of a similar or even larger magnitude to the time-averaged background value. The fluid-turbulence code GRILLIX is extended to use such a global model, which is based on the drift-reduced Braginskii model. The extended model includes electromagnetic and electron-thermal dynamics, and retains global parametric dependencies. Moreover, the Boussinesq approximation, a simplification often employed for numerical reasons, is not justified in the SOL and has been relaxed in GRILLIX. In addition to extending the physical model, the penalisation technique is combined with the flux-coordinate independent (FCI) approach employed in GRILLIX, which allows to study realistic diverted geometries with X-point(s) and general boundary contours, which are in general not conformal with the computational grid. We characterise results from turbulence simulations and investigate the effect of geometry by comparing simulations in circular geometry with toroidal limiter against realistic diverted geometry at otherwise comparable parameters. Turbulence is found to be intermittent with relative fluctuation levels of up to 40% showing that a global description is indeed important. In comparison to circular geometry the fluctuation level is reduced in diverted geometry and has a more complex spatial distribution. Due to local magnetic shear, which is in the edge region fundamentally different between circular and diverted geometry, turbulent structures become distorted and eventually subject to strong perpendicular dissipation. Therefore, the X-point tends to disconnect the high-field from the low-field side, where curvature is unfavourable.

Keywords: Turbulence, scrape-off layer (SOL), flux-coordinate independent (FCI), X-point, separatrix

1. Introduction

Understanding the complex multi-physics of the edge region – the scrape-off layer (SOL) and closed-field line region immediately near the separatrix – is of critical importance for the development of fusion energy. Due to the relative stiffness of the internal profiles of temperature and density, the core values and therefore the overall fusion performance is strongly determined by the edge profiles. Furthermore, in a fusion reactor there will be a large exhaust of particles and heat due to imperfect confinement. This plasma exhaust is directed towards divertor target plates, and preventing these fluxes from exceeding engineering limits, above which the performance and lifetime of the reactor is significantly reduced, is a high-priority area of fusion research. Prediction of these heat fluxes for future devices such as ITER or DEMO is complicated by uncertainty in extrapolation of the width of the exhaust channel from current devices [1, 2].

Modeling of the edge plasma is a significant challenge due to the highly-coupled interplay of multiple different physics regimes and disparate spatial and temporal scales. Magnetized plasma physics, complex magnetic geometry, neutral physics and momentum transfer, atomic and molecular chemistry, radiation from excited states, wall recombination, surface chemistry and impurity sputtering all can affect the edge plasma. Furthermore, the edge can exhibit phenomena over a large range of spatial and temporal scales – from the formation of small-scale intermittent turbulent filaments to large-scale long-timescale effects such as equilibration of the background in response to the magnetic and wall geometry. Inclusion of an extended physics set or finer spatial and temporal scales typically improves the accuracy of the code with respect to experiment, but at the expense of increased computational cost. Within the subset of codes based on the multi-fluid approximation, the two broad classes are 'transport' and 'turbulence' codes. Transport codes such as SOLPS code [3] include a significant range of multi-physics but do not treat turbulent transport self-consistently. Instead, the effects of turbulence are approximated via an effective diffusion, which remains an ad-hoc input. In contrast, turbulence codes self-consistently treat turbulence by evolving the 3D Braginskii models [4] – at the cost of increased runtime and/or a reduced physics set.

Several recent projects aim at developing fluid-turbulence codes, of which we note the GBS [5, 6], HERMES (BOUT++) [7], TOKAM3X [8], GDB [9] and GRILLIX [10] projects. In contrast to the other codes mentioned, the GRILLIX project is notable for its use of the flux-coordinate independent (FCI) approach [11, 12, 13]. This method prevents the issue of coordi-

Email address: Andreas.Stegmeir@ipp.mpg.de (A. Stegmeir)

nate singularities at the separatrix and X-point which arise from the use of field- or flux-aligned coordinates. GRILLIX employs a cylindric grid (R_i, φ_k, Z_j) where parallel operators are discretised via field line tracing between toroidal planes and field line map interpolation within each plane. This allows for the use of a single consistent method to be used for all grid points, including the possibility of (possibly multiple) X-points. Furthermore, the use of Cartesian grids prevents resolution imbalances between the outboard midplane and the X-point region, allowing the dynamics around the X-point to be investigated with high accuracy. To allow for the treatment of general non-conformal boundaries, the penalization method is used to enforce the desired boundary conditions.

In this paper, the extension of GRILLIX by electromagnetic and electron thermal dynamics is presented, with the resulting model being a global drift reduced Braginskii model. Here 'global' means that parametric dependencies are kept and that the Boussinesq approximation is not applied, i.e. nowhere a separation is made between fluctuations and background for the density and temperature. This is needed for the consistent description of high amplitude fluctuations which are regularly observed in experiments [14]. We note that other codes –at least as far as has been reported so far to our knowledge – either use a global model only for simpler (e.g. circular) geometries (e.g. [9]) or treat a more complex geometry but only with a local model, where e.g. the Boussinesq approximation is applied (e.g. [7, 8, 15]). GRILLIX on the other hand can deal with both cases simultaneously, i.e. it retains the full global model even for diverted geometries. A detailed study targeted on the impact of the Boussinesq approximation carried out with GRILLIX in simplified slab geometry is given in [16, 17]. Using parameters characteristic for the COMPASS tokamak [18] turbulence simulations are carried out with GRILLIX. The turbulence features intermittency and exhibits large relative fluctuation levels, which shows that a global description is important. The impact of geometry is studied by comparing simulations in circular geometry with toroidal limiter against realistic diverted geometry at otherwise comparable parameters. The fluctuation level is reduced in diverted geometry and exhibits a more complex spatial distribution. We explain this as a consequence of local magnetic shear, which fundamentally differs in the egde region between circular and diverted geometry. Strong local magnetic shear causes a distortion of turbulent structures, which become subsequently subject to strong perpendicular dissipation. The X-point, where magnetic shear becomes locally very strong, thereby tends to disconnect the low field side from the high field side, where curvature acts stabilizing [19]. Therefore, stronger poloidal asymmetries in the fluctuation level are observed in diverted geometry.

The remainder of this paper is organized as follows: In section 2 we present the physical model employed in GRILLIX, a global 3D drift reduced Braginskii model [20]. With respect to the previous version [10] GRILLIX has been extended by electromagnetic dynamics, electron temperature dynamics and the Boussinesq approximation has been relaxed, which enables to simulate plasma turbulence globally, i.e. without splitting quantities into background and fluctuations. The implementation of important new features is described in section 3. A geometric multigrid solver for the generalised 2D perpendicular Helmholtz equation allows an efficient treatment of the new electromagnetic terms and relaxation of the Boussinesq approximation. The treatment of sheath boundary conditions at the divertor/limiter plates via penalization techniques was motivated from the GDB code [9, 21] and we give a generalisation to diverted geometries. The extended model and new features are verified by analytic means and the method of manufactured solutions (MMS) [22]. In section 4 we characterize edge turbulence with GRILLIX simulations and clarify the impact of geometry by comparing simulations in circular geometry with toroidal limiter against simulations in diverted geometry at otherwise comparable parameters. A summary and outlook is given in section 5.

2. Physical model

2.1. Global drift reduced Braginskii equations

Based on the assumptions of short mean free paths, i.e. $\lambda_c \ll R_0$, the drift reduced Braginskii model describes low frequency ($\omega \ll \Omega_i$) plasma dynamics [20, 4], which is suitable to describe turbulence at low temperature in the edge region self consistently. As further practical approximations cold ions ($T_i \ll T_e$) are yet assumed in GRILLIX, and whereas electromagnetic effects are kept in Ohm's law, the induced magnetic flutter transport is neglected.

The following normalisation is employed: Time t is normalised against R_0/c_{s0} with the sound speed $c_{s0} := \sqrt{T_0/M_i}$ at some reference temperature T_0. Parallel scales $x_\parallel$ are normalised against major radius R_0 and perpendicular scales $x_\perp$ against the sound Larmor radius $\rho_{s0} := c\sqrt{T_0 M_i}/(eB_0)$ with B_0 the magnetic field strength on axis and M_i is the ion mass. The dynamical variables in GRILLIX are density n normalized against some reference density n_0, electron temperature T_e against T_0, parallel ion $u_\parallel$ and electron $v_\parallel$ velocities against c_{s0}, parallel current $j_\parallel$ against en_0c_{s0}, electrostatic potential ϕ against T_0/e and the parallel component of the electromagnetic potential $A_\parallel$ against $\beta_0 B_0 \rho_{s0}$ with $\beta_0 := 4\pi n_0 T_0/B_0^2$ the dynamical plasma beta at reference values. In order to preserve its positivity the logarithms of normalised density $\theta_n := \log n$ and temperature $\xi_e := \log T_e$ are evolved in time. Finally, the normalised set of equations implemented in GRILLIX are:

$$\frac{d_u}{dt}\theta_n + \nabla\cdot(\mathbf{b}u_\parallel) = C(\phi) - T_e\left[C(\xi_e+\theta_n)\right] + \frac{1}{n}\nabla\cdot(\mathbf{b}j_\parallel) + \frac{1}{n}\left[\mathcal{D}_n(n) + S_n\right], \tag{1}$$

$$\nabla\cdot\left[\frac{n}{B^2}\frac{d_u}{dt}\nabla_\perp\phi\right] = -nT_e\left[C(\theta_n+\xi_e)\right] + \nabla\cdot(\mathbf{b}j_\parallel) + \mathcal{D}_w(\Omega), \tag{2}$$

$$\frac{d_u}{dt}u_\parallel = -T_e\left[\nabla_\parallel\theta_n + \nabla_\parallel\xi_e\right] + \mathcal{D}_u(u_\parallel), \tag{3}$$

$$\beta_0 \frac{\partial}{\partial t} A_\parallel + \mu \frac{d_v}{dt}\left(\frac{j_\parallel}{n}\right) = -\left(\frac{\eta_{\parallel 0}}{T^{3/2}}\right) j_\parallel + T_e\left[\nabla_\parallel \theta_n + 1.71 \nabla_\parallel \xi_e\right] - \nabla_\parallel \phi, + \mathcal{D}_p\left(\psi_\parallel\right) \tag{4}$$

$$\frac{d_v}{dt}\xi_e = \frac{2}{3}C(\phi) - T_e\left[\frac{2}{3}C(\theta_n) + \frac{7}{3}C(\xi_e)\right] - \frac{2}{3}\nabla\cdot(\mathbf{b}v_\parallel) + \frac{2}{3}0.71\frac{1}{n}\nabla\cdot(\mathbf{b}j_\parallel)\frac{2}{3}\left(e^{-\frac{5}{2}\xi_e-\theta_n}\eta_{\parallel 0}\right) j_\parallel^2 + \frac{2}{3}e^{-\theta_n-\xi_e}\nabla\cdot\left[\chi_{\parallel 0} e^{\frac{7}{2}\xi_e}\nabla_\parallel \xi_e\right] \frac{1}{T_e}\left[\mathcal{D}_t\left(T_e\right) + S_t\right], \tag{5}$$

$$\nabla_\perp^2 A_\parallel = -j_\parallel. \tag{6}$$

Equations (1-6) are the electron continuity equation, vorticity equation or quasineutrality condition, parallel momentum equation, Ohm's law, electron temperature equation and Faraday's law respectively. The total time derivatives contain advection by the E×B drift and the parallel velocity, i.e. $\frac{d_u}{dt} := \frac{\partial}{\partial t} + (\mathbf{u}_E + u_\parallel \mathbf{b})\cdot\nabla$ and $\frac{d_v}{dt} := \frac{\partial}{\partial t} + (\mathbf{u}_E + v_\parallel \mathbf{b})\cdot\nabla$ with $\mathbf{b} := \mathbf{B}/B$ the unit vector of the magnetic field. As auxiliary variables the generalised vorticity $\Omega := \nabla\cdot\left(\frac{n}{B^2}\nabla_\perp\phi\right)$ and the generalised parallel electromagnetic potential $\psi_\parallel := \beta_0 A_\parallel + \mu\frac{j_\parallel}{n}$ have been introduced. Within the FCI approach (see section 3.1) the advection by E×B velocity and the curvature operator can be written as:

$$\mathbf{u}_E\cdot\nabla f = \frac{\delta}{B^2}\mathbf{B}\times\nabla f \approx -\frac{\delta}{B}\left[\phi, f\right]_{R,Z},$$
$$C(f) = -\delta\left[\left(\nabla\times\frac{\mathbf{B}}{B^2}\right)\cdot\nabla f\right] \approx -2\partial_Z f,$$

with the Jacobi bracket $[\phi, f]_{R,Z} := \partial_R\phi\partial_Z f - \partial_Z\phi\partial_R f$. The dimensionless parameters of the system are the drift scale $\delta := R_0/\rho_{s0}$, electron to ion mass ratio $\mu := \frac{m_e}{M_i}$, the dynamical plasma beta β_0, parallel resistivity at reference $\eta_{\parallel 0} := 0.51\mu/(\tau_{e0}(c_{s0}/R_0))$ with τ_{e0} the electron-ion collision time at reference values and the parallel heat conductivity at reference $\chi_{\parallel 0} := 3.15/\mu\tau_{e0}(c_{s0}/R_0)$. Particle and thermal source terms S_n, S_t have been added, and mostly for numerical reasons also dissipation terms:

$$\mathcal{D}_f := \nu_{\perp,f}\nabla_\perp^{2N} f + \nu_{\parallel,f}\nabla\cdot(\mathbf{b}\nabla_\parallel f), \tag{7}$$

with constant coefficients $\nu_{\perp,f}$, $\mu_{\parallel,f}$, and N controlling the order of perpendicular dissipation. Note that in order to ensure conservation of particles the dissipation in the continuity equation (1) does not act on the logarithm of the density θ_n, but the density n itself.

The model is global in the sense that no separation of variables between a background part and fluctuating part is made and the dependency of the parallel resistivity and heat conduction on density and temperature is kept. Moreover the dependency on the density in the polarization term of the vorticity equation (2) is also kept, i.e. the Boussinesq approximation is not applied. The model conserves energy apart from the fact that we have neglected advection by the polarization velocity, which has been shown to have only a minor effect on conservation of energy [23].

2.2. Boundary conditions

The simulation domain in GRILLIX is usually bounded by an inner (core) limiting flux surface, an outer (wall) limiting flux surface and depending on geometry by limiter or divertor baffle plates.

Sheath physics determining the boundary conditions for the divertor/limiter is a rich topic by itself, especially in the case of glancing angles between magnetic field and target plate. A sophisticated set of boundary conditions is discussed e.g. in [24], but our boundary conditions originate from standard Bohm sheath boundary conditions [25]:

$$u_\parallel \gtrless \pm\sqrt{T_e}, \tag{8}$$

$$j_\parallel = n u_\parallel \mp n\sqrt{T_e}\exp\left[\Lambda - \max\left(\frac{\phi}{T_e}, 0\right)\right], \tag{9}$$

$$-\chi_\parallel\nabla_\parallel T_e = \gamma_e T_e u_\parallel, \tag{10}$$

where the upper/lower sign denotes if the direction of magnetic field is directed towards/away from target plates, $\Lambda \approx 0.5\ln\left(\frac{M_i}{2\pi m_e}\right)$ is the sheath floating potential and $\gamma_e \approx 2.5$ the effective electron sheath transmission factor. We limit the electron flow into the sheath as was also done in [7, 15], and there is also the option to run with insulating sheath boundary conditions:

$$j_\parallel = 0, \quad \phi = \Lambda T_e,$$

The treatment of sheath boundaries within the FCI approach is numerically cumbersome for which a penalization method is employed described in section 3.2.

In the radial direction either homogeneous Neumann boundary conditions (for n, T_e, $u_\parallel$) are applied or homogeneous Dirichlet boundary conditions (for $A_\parallel$, $j_\parallel$, Ω). An exception is the electrostatic potential which is set at the wall to $\phi|_{wall} = \Lambda T_e$. In order to avoid fluxes of energy and particles due to $E\times B$ drifts through the core, the potential has to be constant on the inner limiting flux surface, and we set it to $\phi_{core} = \Lambda\langle T_e\rangle_{LCFS}$, where $\langle T_e\rangle_{LCFS}$ is the zonal averaged electron temperature on the last closed flux surface. The motivation for this stems from the fact that due to the sheath boundary conditions the potential follows roughly $\phi \sim \Lambda T_e$ in the SOL, and the chosen boundary condition does therefore not allow a global radial electric field in the closed flux surface region. The large scale radial electric field in the closed field line region is determined by effects that are not yet included in the GRILLIX model, e.g. ion pressure gradient [26, 27]. Therefore, the self-consistent modeling of the global radial electric field in the closed field line region is postponed until at least ion temperature effects will be taken into account in GRILLIX. We want to note that from the geometrical point of view GRILLIX is able to deal easily with the full tokamak including the core region with O-point [10]. Whereas this

would exclude a possibly spurious influence from core boundaries and therefore allow a more self-consistent approach, it is currently of low practical interest due to the large computational overhead caused by the many additional grid points.

3. GRILLIX

3.1. Spatial discretisation

GRILLIX is based on the FCI approach [11, 12, 13] in a toroidally staggered framework which is described in detail in [10] and is therefore here only reviewed very shortly. For tokamak geometries a cylindric grid (R_i, φ_k, Z_j) is employed being Cartesian within poloidal planes. Based on the assumption of strong toroidal field ($B_{pol}/B_{tor} \ll 1$), the discretisation of perpendicular operators remains within poloidal planes for which second order finite difference methods are used. The Jacobi bracket is discretised according to the Arakawa scheme [28] and the discretisation of the non-linear polarization term in eq. (2) is described in [23]. The discrete parallel gradient is computed at toroidally staggered positions $\varphi_{k+\frac{1}{2}}$ according to a finite difference along magnetic field lines (see fig. 1):

$$\nabla_\parallel f_{i,k+\frac{1}{2},j} := \frac{f_{k+1}\left(\boldsymbol{\gamma}_{i,j}\left(\frac{\Delta\varphi}{2}\right)\right) - f_k\left(\boldsymbol{\gamma}_{i,j}\left(-\frac{\Delta\varphi}{2}\right)\right)}{s_{i,j}\left(\frac{\Delta\varphi}{2}\right) + s_{i,j}\left(-\frac{\Delta\varphi}{2}\right)},$$

where $\boldsymbol{\gamma}_{i,j}(\varphi)$ is the poloidal projection of the characteristic along field line and $s_{i,j}(\varphi)$ the associated length along field line defined as the solution of the following ordinary differential equations which are solved via a Runge-Kutta integrator [29]:

$$\frac{d\boldsymbol{\gamma}_{i,j}}{d\varphi} = \frac{1}{B^\varphi}\begin{pmatrix} B^R \\ B^Z \end{pmatrix}, \qquad \text{with: } \boldsymbol{\gamma}_{i,j}(0) = \begin{pmatrix} R_i \\ Z_j \end{pmatrix},$$
$$\frac{ds_{i,j}}{d\varphi} = \frac{|B|}{B^\varphi}, \qquad \text{with: } s_{i,j}(0) = 0,$$

i.e. corresponding map points are computed by tracing along magnetic field lines. The values on map points are obtained from a 3rd order bi-polynomial interpolation within the poloidal planes φ_k and φ_{k+1}. We note that the magnetic field is assumed axisymmetric in GRILLIX, which is however not a general constraint for the FCI approach [30, 31]. In the same spirit operators are established that map quantities between the grid and the staggered dual grid and vice versa. The parallel divergence operator $\nabla \cdot (\mathbf{b} f)$ is obtained in its discrete version via the support operator method [32, 33] as described in [10]. The structure of the equations suggest that $n, \theta_n, \xi_e, T_e, \phi$ and Ω are collocated to the canonical grid whereas $u_\parallel, v_\parallel, j_\parallel, A_\parallel$ and $\psi_\parallel$ are collocated to the staggered grid.

3.2. Penalization for sheath boundary conditions

The boundaries at the sheath are in general neither conformal with the grid nor aligned with the exceptional parallel direction along the magnetic field line, which makes their treatment numerically difficult and cumbersome. In such situations penalization techniques have proven themselves also for plasma fluid codes [34, 35]. A combination of the FCI with penalization was firstly employed in GDB for limited plasmas [9, 21] and we implemented in GRILLIX a generalization allowing to deal also with diverted plasmas.

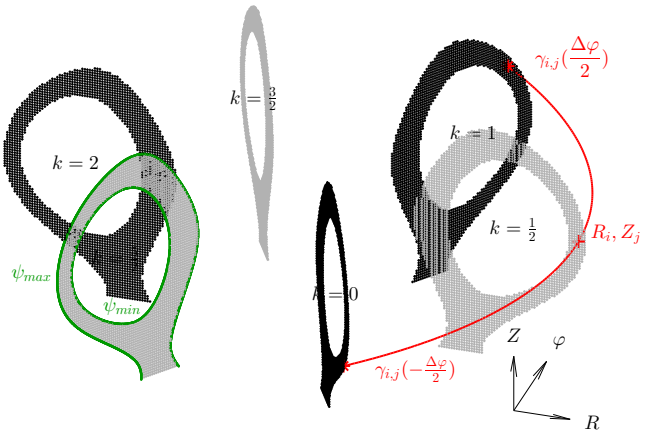

Figure 1: Scheme for toroidally staggered FCI. A cylindric grid (R_i, φ_k, Z_j) is used spanning the simulation domain by a set of Cartesian poloidal planes bounded by limiting flux surfaces (ψ_{min}, ψ_{max}). In addition to the canonical grid (black, $k = 0, 1, 2, \dots$) a toroidally staggered dual grid (gray, $k = \frac{1}{2}, \frac{3}{2}, \frac{5}{2}, \dots$) is introduced. The parallel gradient is discretised via field line tracing and interpolation and maps from the canonical grid to the staggered grid.

Equations (1-5) are each modified according to:

$$\frac{\partial}{\partial t} f = (1-\chi) F_f + \frac{\chi}{\epsilon}(f_P - f), \tag{11}$$

where f represents here the dynamical variables respectively and F_f the corresponding terms according to the Braginskii model. χ is a characteristic function, which is 0 in the physical domain and 1 in the boundary region, where we choose in practice a smooth transition [34] across the boundary based on tanh functions (see fig. 5 left column for examples). $\epsilon \ll 1$ is the penalization parameter such that in the region where $\chi \approx 0$ eq. (11) approximates the original physical equation, whereas in the region $\chi \approx 1$ the variable f is strongly damped to a prescribed function f_P. Via suitable choice for f_P different boundary conditions can be realized.

As an illustrative example we discuss here our implementation for general Neumann boundary conditions, i.e.:

$$\nabla_\parallel f\big|_{sheath} = \alpha.$$

Firstly, we define an additional function ζ, which is 1 in the penalization region where the magnetic field is pointed towards the target and -1, where the magnetic field is pointed away from the target with possibly, i.e. in toroidal limiter geometry, a smooth transition between both regions (see fig. 5 right column for examples). Secondly, we denote for some grid point $f^\pm := f_{k\pm1}\left(\boldsymbol{\gamma}_{i,j}(\pm\Delta\varphi)\right)$ the values on its map points which are again obtained via interpolation within adjacent planes and $s^\pm := s_{i,j}(\pm\Delta\varphi)$ the associated lengths along field line. The penalization value is then prescribed as:

$$f_P = \begin{cases} |\zeta|\,(f^- + s^-\alpha) + (1-|\zeta|)\frac{f^+ + f^-}{2} & \text{for: } \zeta \geq 0, \\ |\zeta|\,(f^+ - s^+\alpha) + (1-|\zeta|)\frac{f^+ + f^-}{2} & \text{for: } \zeta < 0. \end{cases} \tag{12}$$

The first terms set the actual boundary condition and use the values obtained from the field line map towards the interior domain. The second terms ensure for toroidal limiter geometries a continuous transition between both limiter sides.

3.3. Time stepping

The equations are advanced in time with the 3rd order Karniadakis scheme [36]. Only the penalization term that is directly proportional to the quantity itself is treated fully implicit in time, i.e. the equations written in the form of eq. (11) are discretised in time according to:

$$f^{t+1}\left(11 + 6\Delta t\frac{\chi}{\epsilon}\right) = \sum_{i=0...2} a_i f^{t-i} + b_i \Delta t\left[\left(1-\frac{\chi}{\epsilon}\right)F^{t-i}(f^{t-i}) + \frac{\chi}{\epsilon}f_P^{t-i}\right],$$

with $a_0 = 18$, $a_1 = -9$, $a_2 = 2$ and $b_0 = 3$, $b_1 = -3$, $b_2 = 1$. The solution for f^{t+1} is trivial as the implicit penalization term on the left hand side is diagonal.

3.4. Elliptic solver

In order to compute the electrostatic potential ϕ from eq. (2) and the parallel electromagnetic potential $A_\parallel$ from eqs. (4) and (6) two Helmholtz type equations have to be solved in each time-step within each poloidal plane:

$$\lambda f - \nabla\cdot(c\nabla_\perp f) = b, \tag{13}$$

with given right hand side b, and coefficients λ and c. In the global model the coefficients have in generally a spatio-temporal dependency, where direct solvers become very inefficient as a costly matrix LU-decomposition would have to be performed in each time-step. An efficient solution technique for eq. (13) is provided by geometric multigrid methods [37], which is implemented in GRILLIX based on a damped Jacobi smoother with trivial restriction and bilinear prolongation.

3.5. Verification

One of the main new features in GRILLIX are electromagnetic and electron inertial effects in Ohm's law, which gives rise to shear Alfvén dynamics. The core model for the shear Alfvén wave is obtained by linearizing equations (1-6) in the isothermal limit ($T_e = 1$), neglect curvature, parallel ion velocity ($u_\parallel = 0$) and parallel resistivity $\eta_{\parallel 0} = 0$. In this limit a wave equation is obtained [38] for the 'non-adiabaticity' $(\tilde{n}-\tilde{\phi})$, where the tilde denotes a fluctuating quantity.

$$\frac{\partial^2}{\partial t^2}\left(\tilde{n}-\tilde{\phi}\right) = v_{SAW}^2\nabla_\parallel^2\left(\tilde{n}-\tilde{\phi}\right), \tag{14}$$

with $\mathrm{v}_{SAW}^2 = (1+k_\perp^2)/(\beta_0+\mu k_\perp^2)$ the phase velocity of the shear Alfvén wave, where $k_\perp$ is the perpendicular mode number. In the limit $k_\perp \ll 1$ the wave propagates at the Alfvén speed $v_A = \beta_0^{-1/2}$ and in the limit $k_\perp \gg 1$ at the electron thermal speed $v_{Te} = \mu^{-1/2}$. In order to verify the implementation of the electromagnetic and electron inertia effects we perform simulations with GRILLIX in a 3D periodic slab ($C = 0$) without the parallel momentum equation (3) and electron thermal equation (5), but set $T_e = 1$ and $u_\parallel = 0$. Otherwise we run the global version of the code but initialize the density with constant background plus a fluctuation of small amplitude $\frac{\tilde{n}}{n_{bck}} = 0.1$ being a mode structure in the perpendicular plane and a Gaussian along the parallel direction. The phase velocity of the divergent wave along the magnetic field is measured and compared to the analytic prediction for v_{SAW}. The result shown in fig. 2 shows an excellent agreement between GRILLIX simulations and the analytic prediction.

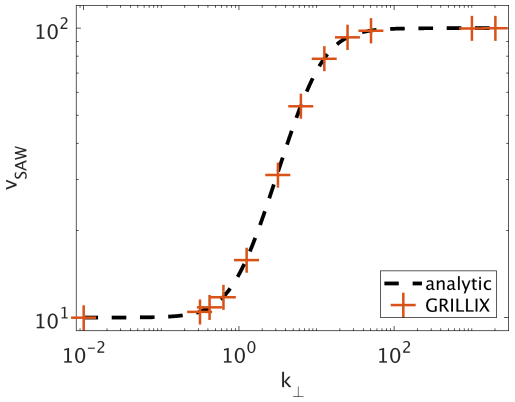

Figure 2: Velocity of shear Alfvén wave obtained with GRILLIX against analytic prediction for fixed $\beta_0 = 1\cdot 10^{-2}$ and $\mu = 1\cdot 10^{-4}$ in dependence of $k_\perp$

	k_ρ	$(k_\theta, \delta\theta)$	$(k_\varphi, \delta\varphi)$	ω
θ_n	1	(1, 0)	(1, 0)	100
ξ_e	1	(1, 1.5)	(1, 0.5)	73
ϕ	2	(2, 0)	(1, 0)	80
$u_\parallel$	3	(1, 0)	(1, 0)	65
$A_\parallel$	2	(1, 0)	(1, 0)	88

Table 1: Parameters for analytic MMS functions used as inputs for different dynamical fields.

A verification of the full system via the Method of Manufactured Solution (MMS) [22] was performed in circular geometry with purely closed flux surfaces. The same setup and procedure as described in [10] for the previous simplified set of equations is applied here to the global model. The analytic MMS functions are prescribed for each dynamical field as a product of radial (k_ρ), poloidal (k_θ with phase shift $\delta\theta$), toroidal (k_φ with phase shift $\delta\varphi$) and temporal (ω) modes (see table 1). The analytic MMS functions are quite general for GRILLIX, as its numerical approach is independent of flux surfaces. The numerical error of the MMS analysis for all dynamical fields in dependence of resolution is shown in fig. 3 and follows a second order convergence, which is a good indication for correct implementation of the equations in GRILLIX.

Finally, we want to note that also a validation in slab geometry based on experiments in the Large Plasma Device (LAPD) was performed for which results can be found in [16, 17].

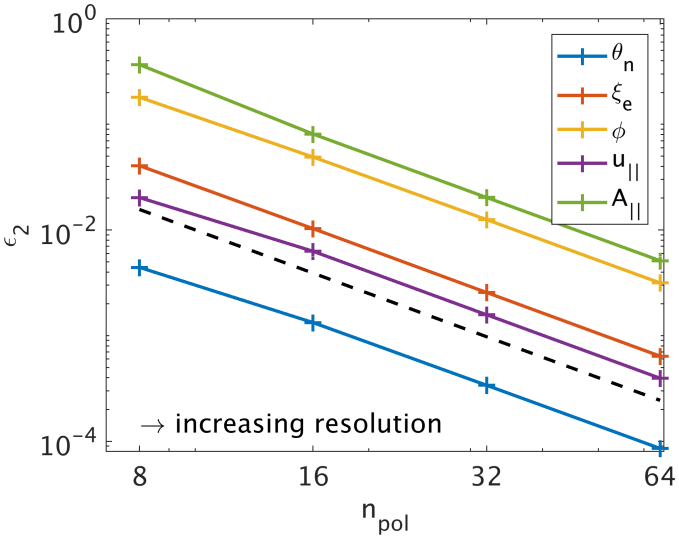

Figure 3: Numerical error of MMS verification procedure for different dynamical fields evolved in GRILLIX. Error is measured in L2-norm, i.e. $\varepsilon_2 = |u_{num} - u_{mms}|_2 \,/\, |u_{mms}|_2$ at $t = 0.2$. Black dashed lines indicates second order convergence for reference. Resolution is subsequently doubled in all directions starting at the coarsest level with $n_{pol} = 8$ poloidal planes, $h = 3 \cdot 10^{-3}$ and $\Delta t = 1 \cdot 10^{-4}$.

4. Simulation results

4.1. Setup

The parameters for our simulations are motivated from experiments with deuterium plasma in the COMPASS tokamak [18], where we normalise density and temperature to upstream separatrix values:

$$R_0 = 56\,\text{cm}, \qquad a_{min} = 20\,\text{cm}, \qquad B_0 = 1.2\,\text{T},$$
$$n_0 = 1 \cdot 10^{13}\,\text{cm}^{-3}, \qquad T_0 = 30\,\text{eV},$$

with a_{min} the minor radius. This corresponds to the following dimensionless input parameters for GRILLIX:

$$\beta_0 = 1.68 \cdot 10^{-4}, \qquad \delta = 849, \qquad \mu = 2.72 \cdot 10^{-4},$$
$$\chi_{\parallel 0} = 340, \qquad \eta_{\parallel 0} = 4.72 \cdot 10^{-3}.$$

The strongest time-step limitation stems from the parallel electron heat conduction, and by linearizing this term we may anticipate a rough scaling for the time-step of $\Delta t \lesssim \frac{n}{\chi_{\parallel 0} T^{5/2}} \Delta\varphi^2$ with $\Delta\varphi$ the toroidal grid distance between adjacent planes. In order to perform simulations at a larger time-step we employ in our simulations presented here mostly a reduced heat conductivity of $\chi_{\parallel 0} = 20$, but still retain the parametric dependency on temperature ($\propto T^{5/2}$). Correspondingly, we also use a reduced value for the effective sheath transmission factor of $\gamma_e = 0.15$. In section 4.4 we investigate the effect of this by comparing to a run with more realistic heat conductivity. Development towards relaxation of the time-step limitation by an implicit treatment of parallel electron heat conduction is targeted for future work.

We performed simulations in circular geometry with toroidal limiter and diverted geometry at otherwise comparable parameters. The background magnetic field for the diverted geometry

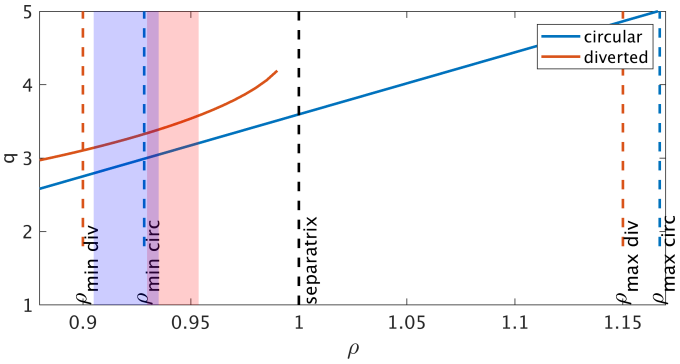

Figure 4: Safety factor q as function of normalised radial coordinate ρ for circular and diverted geometry. The limiting flux surfaces are indicated with dashed blue respectively green lines and the source regions with colored shaded areas.

is given in terms of an analytic flux function $\psi(R, Z)$ from the class of solutions described in [39] with parameters chosen as described in [40]. We define as normalised radial coordinate $\rho = \sqrt{\frac{\psi - \psi_0}{\psi_X - \psi_0}}$, where ψ_0, ψ_x is the poloidal magnetic flux at magnetic axis respectively at separatrix. For circular geometry we define equivalently the normalised radial coordinate as $\rho := \frac{\sqrt{(R-R_0)^2 + Z^2}}{a_{min}}$ and the magnetic field is given in terms of a prescribed safety factor profile $q(\rho)$. The setup for the simulations in terms of radial view is shown in fig. 4. The sheath boundary conditions are treated via a penalization approach and the characteristic function χ prescribing the location of the sheath is illustrated for both geometries in fig. 5. We employ yet insulating sheath boundary conditions as they were found to be more robust.

The simulations are driven via particle and energy source terms of the form

$$S_{n,T} = c_{n,T} \exp\left(-\frac{(\rho - \rho_{n,T})^2}{w_{n,T}^2}\right)\Big(\langle n, T\rangle_\rho - f_{n,T}\Big),$$

i.e. the sources drive the zonal averaged density $\langle n\rangle_\rho$ respectively temperature $\langle T\rangle_\rho$ towards target values $f_{n,T}$, where $c_{n,T}$ is the rate, $\rho_{n,T}$ location and $w_{n,T}$ the radial width of the source.

The main simulations analyzed in section 4.2 and 4.3 were run with 32 poloidal planes, perpendicular resolution of $h = 1\,[\rho_{s0}]$ corresponding to 0.066 cm and a time-step of $\Delta t = 5 \cdot 10^{-5}\,[R_0/c_{s0}]$. The total number of grid pints were $\approx 5.0 \cdot 10^6$ grid points for the circular case and $\approx 14 \cdot 10^6$ for the diverted case. A sixth order hyperviscosity ($\nu_{\perp,f} \nabla_\perp^6$) is applied in the perpendicular direction and regular diffusion ($\mu_{\parallel,f} \nabla \cdot (\mathbf{b}\nabla_\parallel)$) in the parallel direction, where the coefficients were chosen as $\nu_{\perp,f} = 10$ and $\mu_{\parallel,f} = 0.025$ cutting off turbulent spectra by smoothing structures on the grid scale. The independence of the results from these numerical parameters was checked at the circular case (see section 4.4). The radial extent of the simulations in circular geometry is $\sim$ 1.5 cm (edge) + 3.5 cm (SOL) and in diverted geometry $\sim$ 1.5 cm (edge) + 2.3 cm (SOL) at outboard midplane respectively $\sim$ 3.2 cm (edge) + 5.5 cm (SOL) at inboard midplane.

The simulations were initialized with uniform background in density and temperature (0.2) plus small random noise (0.01).

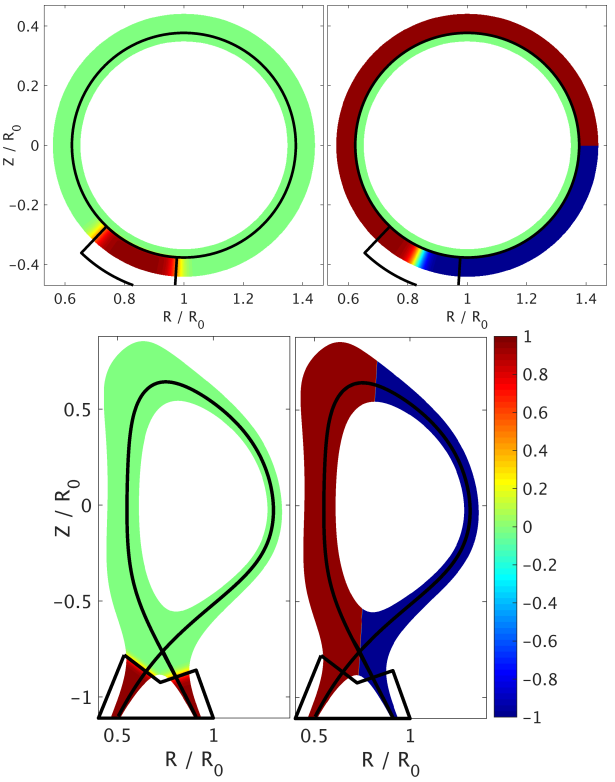

Figure 5: Penalization functions χ (left) and ζ (right) used in circular (top) and diverted (bottom) geometry. Black lines indicate separatrix and limiter respectively divertor target plates.

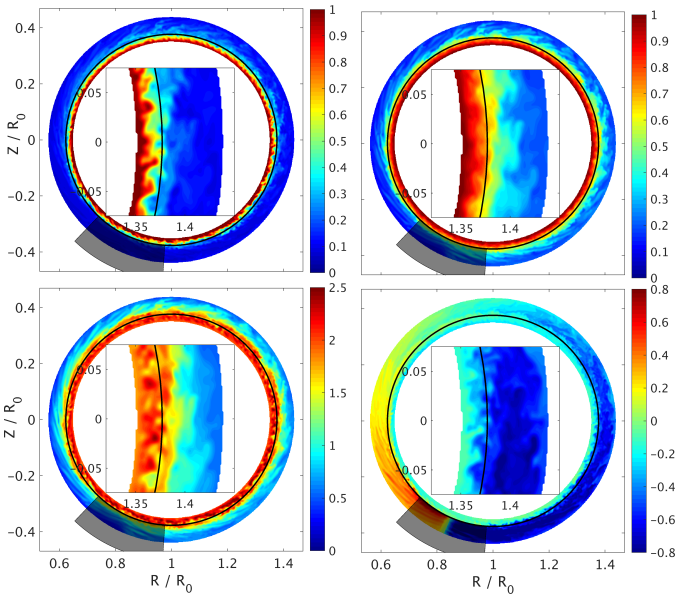

Figure 6: Snapshots of density (top left), electron temperature (top right), electrostatic potential (bottom left) and parallel ion velocity (bottom right) in circular geometry. Insets show outboard midplane region enlarged. Solid black line indicates last closed flux surface and gray shaded area penalization region due to toroidal limiter.

Particles and energy are injected via the sources, and the simulations enter saturated phase, which is independent of the initial state (for the circular case around $t \approx 30$) from where data is collected for performing statistical analysis. The overall simulation time for the circular case was up to $t = 77$, corresponding to $\approx$ 1ms. The simulations were carried out on the Marconi-A2 (KNL) partition on 16 nodes (2 MPI processes times 34 cores per node). Within 24 hours GRILLIX ran a normalised time interval of $\approx 10\,[R_0/c_{s0}]$ for the circular case and $\approx 4\,[R_0/c_{s0}]$ for the diverted case.

4.2. Circular geometry

Snapshots of density, electron temperature, electrostatic potential and parallel velocity for the circular geometry with toroidal limiter are shown in fig. 6. There is a clear difference between the closed field line region and the SOL, which is dominated by the Bohm boundary condition for the parallel velocity. Blob-like structures in the density can be observed around the last closed flux surface.

Time traces of pressure during the saturated state at low (LFS) and high (HFS) field side midplane are shown in fig. 7a. Especially the LFS-signal is highly intermittent with fluctuations of up to 200%, implying that a global model, which does not rely on a splitting into fluctuations and background, is indeed important. The fluctuation level on the HFS is lower which results from the ballooning character of the turbulence where curvature acts stabilizing at HFS and destabilizing at LFS. It has been found that turbulence in the SOL of limited plasmas is driven by resistive ballooning modes [41, 42] with linear growth rates somewhat smaller than the interchange growth rate $\gamma_I = \sqrt{2R_0/L_p}$, where L_p is the background pressure gradient length. Via the autocorrelation we may gain some insight into the characteristic time scales of the turbulent dynamics, which is computed discretely and in normalised form as:

$$A_f(\tau_i) := \frac{\sum_n f(t_n) f(t_{n-i})}{\sum_n f(t_n)^2},$$

with $f(t_n)$ the signal at discrete time point t_n. The autocorrelation function for the pressure at LFS is shown in fig. 7b. A correlation time in the order of $\tau_c \approx 0.5 \ldots 1$ maybe deduced, although the initial decay is not strictly exponential. The characteristic turbulent time scales are therefore larger than the interchange time scale $t_I = \gamma_I^{-1} \approx 0.08$, where the pressure gradient length in the edge has been estimated from the self-consistently obtained profiles (see fig. 8c) as $L_p/R_0 \approx 0.012$. The turbulence is therefore compatible to be driven by resistive ballooning modes.

Furthermore, we analyse the simulation by computing profiles $\langle f \rangle$, fluctuation levels $\delta f = \left\langle f^2 - \langle f \rangle^2 \right\rangle^{1/2}$ and skewness $\left\langle f^3 - \langle f \rangle^3 \right\rangle / \delta f^3$, where angular brackets denote an average over toroidal direction and time within the saturated phase. Our statistical analysis was robust against averaging over different time windows. In fig. 8 profiles of density, electron temperature and pressure are shown with the corresponding fluctuation levels and in fig. 9 the relative pressure fluctuation level and skewness of pressure. There is a kink in the density and pressure at the last closed flux surface and a little distance outside

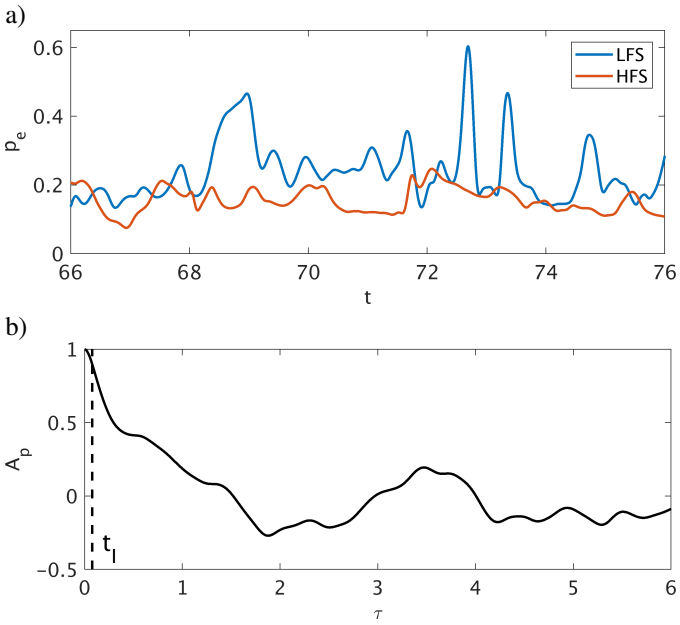

Figure 7: a) Time traces of pressure on the last closed flux surface ($\rho = 1.0$) at low (LFS) and high (HFS) field side midplane positions for circular limited geometry. b) Corresponding autocorrelation function for low field side signal. Dashed line indicates characteristic time-scale related with growth rate of interchange instability $t_l = \sqrt{L_p/(2R_0)}$.

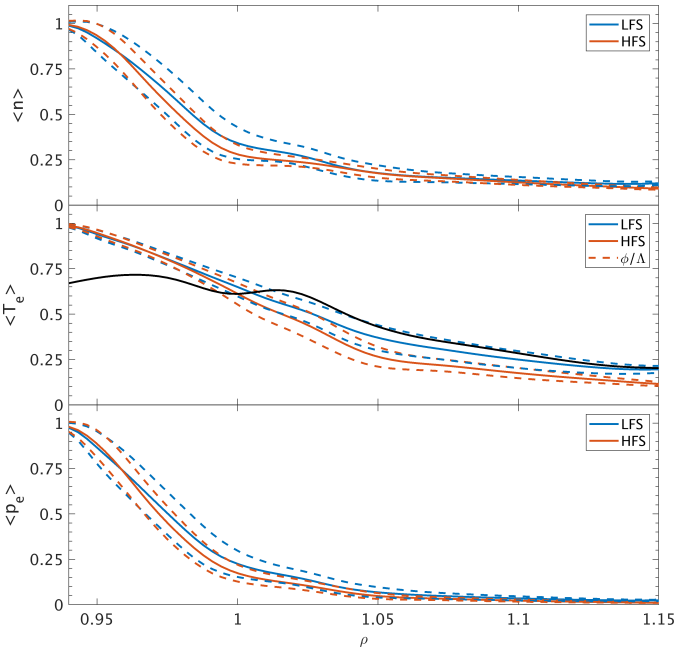

Figure 8: Radial cut of density (top), electron temperature (center) and pressure (bottom) profiles at low field side (LFS) and high field side (HFS) for circular geometry. Dashed lines indicate fluctuation amplitude added to and subtracted from profiles. At the profile for the electron temperature the averaged ϕ/Λ at LFS is additionally plotted as black line.

also for the temperature at $\rho \approx 1.05$. The electrostatic potential follows in the SOL $\phi \approx \Lambda T_e$ and deviates from this in the closed field line region where the potential at the inner limiting flux surface is prescribed as $\phi|_{\rho_{min}} = \langle \Lambda T_e \rangle_{\rho=1}$. There is a small difference in profiles and fluctuation levels between low field side and high field side, where profiles are steeper and the fluctuation level is slightly lower due to favourable curvature. The relative fluctuation level (see fig. 9a) increases from the edge towards the separatrix and is in the SOL on a level of around $30-40\%$, which substantiates again the importance of a global model. The skewness (see fig. 9b) approaches zero in the region of strong pressure gradients, which is an indication for a Gaussian probability density function and uncorrelated turbulence, and it becomes positive in the SOL, which is an indication for the presence of blobs.

4.3. Comparison with diverted geometry

Snapshots for the diverted case are shown in fig. 10, where again a clear distinction between closed field line region, SOL and private flux region in the dynamics is obvious. From the snapshots there seems to be a qualitative difference with respect to circular geometry: The turbulence is generally more quiescent especially in the SOL and we do not identify blobs at outboard midplane as clearly as in circular geometry.

Firstly, we consider again time traces of pressure at different poloidal positions at the separatrix in fig. 11. In comparison to circular geometry (see fig. 7a) the dynamics is more quiescent with smaller fluctuations and the poloidal asymmetry is stronger pronounced, i.e. fluctuations at HFS are much weaker than at LFS and at the X-point. The poloidal asymmetry becomes also obvious from fig. 12, where the pressure fluctuation

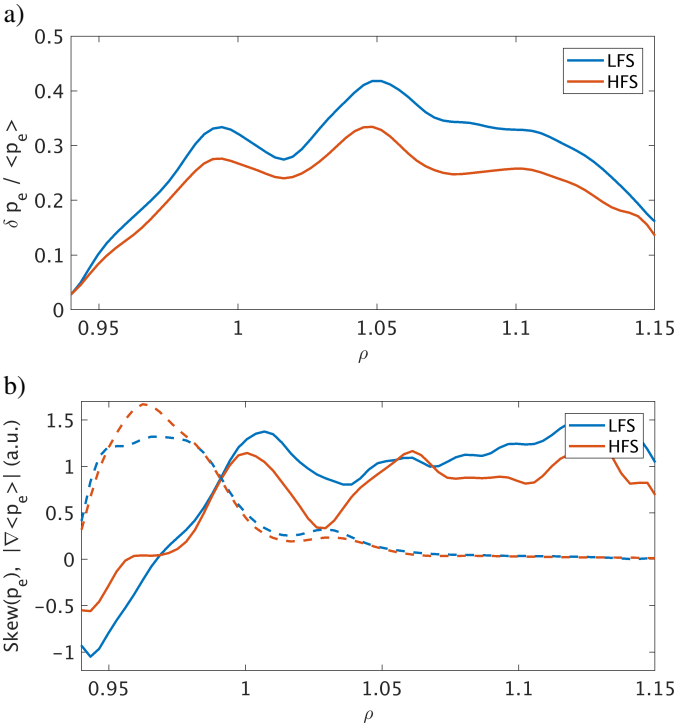

Figure 9: a) Relative pressure fluctuation level $\delta p_e / \langle p_e \rangle$ and b) skewness of pressure for circular geometry. Dashed lines in (b) show additionally pressure gradient $|\nabla \langle p_e \rangle|$ in arbitrary units.

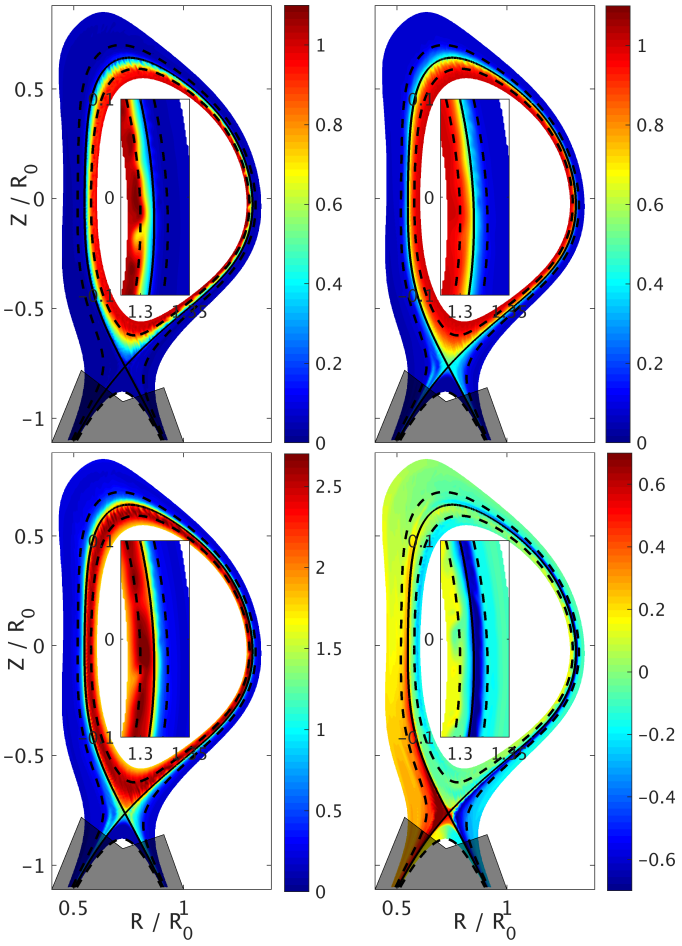

Figure 10: Snapshots of density (top left), electron temperature (top right), electrostatic potential (bottom left) and parallel ion velocity (bottom right) in diverted geometry at $t = 48.25$. Insets show outboard midplane region enlarged. Solid black line indicates separatrix, dashed black lines flux surfaces $\rho = 0.95$ and $\rho = 1.05$ as reference. Gray shaded area marks penalization region due to divertor plates.

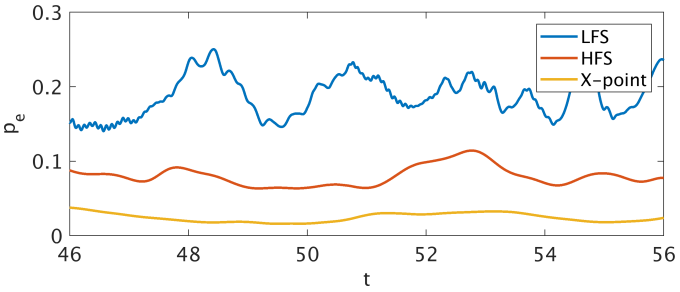

Figure 11: Time traces of pressure on the separatrix at different poloidal positions for diverted geometry.

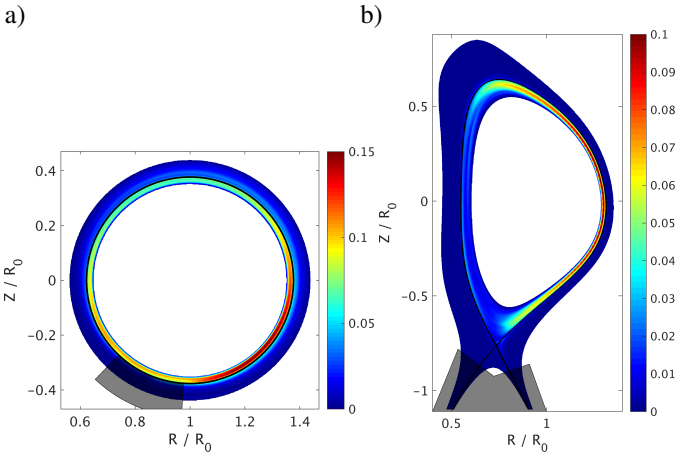

Figure 12: Pressure fluctuation level δp_e for a) circular geometry and b) diverted geometry.

is shown in poloidal cross section. In the edge region of the circular geometry the pressure fluctuation level varies on a flux surface within a factor of two, whereas in diverted geometry the fluctuation level varies within a flux surface from LFS towards HFS by an order of magnitude. Especially in the vicinity of the X-point there is a strong drop in the fluctuation level towards HFS.

To give a reason for the stronger poloidal asymmetries in diverted geometry we investigate the effect of magnetic geometry on turbulent fluctuations and consider the local magnetic shear:

$$s_{loc}(\theta, \rho_N) = \frac{\partial}{\partial \rho}\left(\frac{B^\varphi}{B^\theta}\right),$$

where $\tan\theta := Z/(R - R_0)$ is the geometric poloidal angle. A plot of the local magnetic shear for flux surfaces just inside the separatrix is shown in fig. 13. Whereas the local shear is obviously constant in circular geometry, it follows a complicated course in diverted geometry, i.e. it is very low in the outboard midplane region, increases towards the top and high field side region and approaches a singularity at the X-point. Turbulent structures, which are driven in the outboard midplane region due to unfavourable curvature, become distorted in the perpendicular direction due to local magnetic shear (see also [43]). Being strongly distorted, i.e. especially in the vicinity of the X-point, they become subject to perpendicular dissipation damping fluctuations. Therefore the X-point ultimately acts as

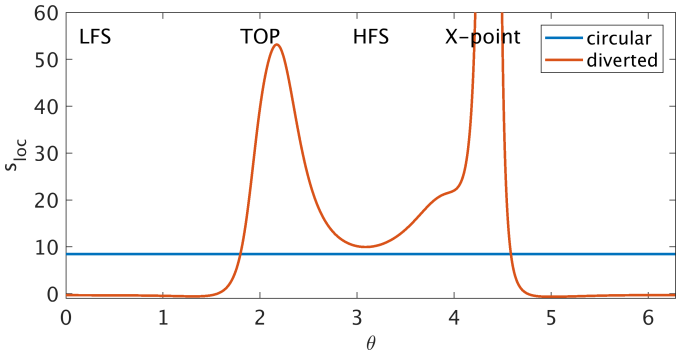

Figure 13: Local magnetic shear s_{loc} on flux surface $\rho = 0.992$ close to separatrix for circular and diverted geometry as function of geometric poloidal angle.

kind of barrier for fluctuations [19] (See also resistive X-point mode by Myra et al. [44]). This explains the drop of the fluctuation level near the X-point towards HFS in our simulation (see fig. 12b). The same mechanism in an alleviated explains also the drop in fluctuation level towards HFS near the top region, where local magnetic shear is also high.

In contrast to flux-aligned approaches GRILLIX does not suffer from coordinate singularity and a loss of resolution near the X-point due to flux expansion, but the FCI approach allows an accurate treatment of the dynamics around the X-point. A detailed view of the pressure at the X-point is shown in fig. 14a. Fluctuations approaching the X-point fan out radially becoming ever narrower in the poloidal direction, which illustrates the mechanism described in the previous paragraph. A Quiescent X-point Region (QXR) directly next to the X-point in the SOL was observed in MAST experiments [45]. It was argued that the QXR results from quiescence in local plasma conditions close to the X-point, and the QXR was found to be ubiquitous to MAST plasmas bounded between the separatrix and the $\psi_N = 1.02$ flux surface. In order to see if this phenomenon appears at least qualitatively also in our simulations we give a detailed view on the pressure fluctuation level in the direct vicinity of the X-point in fig. 14b. The pattern of the pressure fluctuation level around the X-point is complex and the result is ambiguous. Our statistical analysis was checked to be robust against averaging over different time frames, but statistical noise due to insufficient data or resolution cannot fully be excluded in this dynamically sensitive region. We observe only a very narrow region between the separatrix and the $\rho = 1.003$ flux surface that could be an indication for the QXR. However, the situation might change and become clearer if we considered plasma parameters and magnetic geometry closer to MAST.

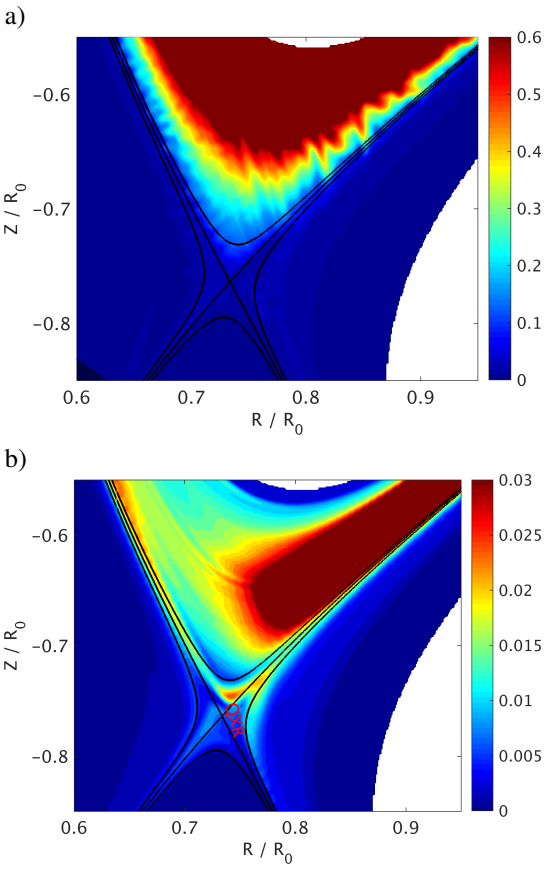

Figure 14: Detailed view on X-point. Solid lines indicate flux surfaces $\rho = 0.997, 1.0, 1.003$. a) Snapshot of pressure where the distortion of structures towards the X-point is visible. b) Pressure fluctuation level. The region in the SOL directly next to the X-point might indicate the Quiescent X-point Region (QXR) described in [45].

4.4. Convergence analysis and impact of heat conductivity

A posteriori, we subject our results to a convergence check and study the impact of heat conductivity, as we decreased it artificially.

For a convergence check we ran the circular case at nominal resolution, at half resolution and at a resolution that was increased by a factor of one third. We correspondingly adapted also other numerical parameters, i.e. we decreased numerical dissipation coefficients with increasing resolution. Moreover,

	$h_\perp$	N_{pol}	ν	μ	w_θ	w_ρ
coarse	2.0	16	500.0	$5.0 \cdot 10^{-2}$	0.1	$6.0 \cdot 1($
nominal	1.0	32	10.0	$2.5 \cdot 10^{-2}$	$7.5 \cdot 10^{-2}$	$4.0 \cdot 1($
fine	0.67	48	2.0	$1.5 \cdot 10^{-2}$	$5.0 \cdot 10^{-2}$	$3.0 \cdot 1($

Table 2: Numerical parameters used for convergence check. w_θ is poloidal decay length in radians and w_ρ radial decay length in units of R_0 for penalisation function, which is parametrized via tanh functions.

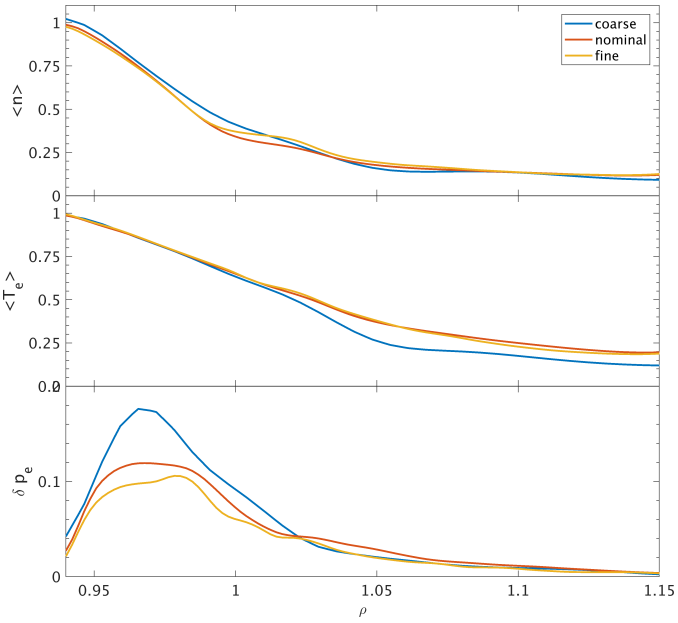

Figure 15: Result of convergence analysis: Outboard midplane profiles for density (top), electron temperature (center) and pressure fluctuation level (bottom) obtained with coarse, nominal and fine resolution.

we also varied the poloidal and radial decay lengths of the penalisation functions χ in order to exclude spurious effects from our penalisation approach. The numerical parameters employed are listed explicitly in table 2. The obtained profiles and pressure fluctuation level at LFS are shown in fig. 15. Whereas there is a deviation in the temperature profile to the coarse resolution case, the fine and nominal resolution match here very well. The density profiles between nominal and fine resolution match overall well apart from the density shoulder at $\rho = 1$ which is slightly more pronounced at finer resolution. Also the pressure fluctuation converges and deviation between nominal and fine resolution could also be owed to the fact that for the fine case not as much statistics as for the other cases was available due to computational constraints.

Compared to realistic COMPASS parameters we employed a significantly reduced artificial heat conductivity of $\chi_{\parallel 0} = 20$ instead of $\chi_{\parallel 0} = 340$ and correspondingly also decreased the effective sheath transmission factor to $\gamma_e = 0.15$ instead of $\gamma_e = 2.5$. In order to study the effect of this we restarted with reduced time-step the circular limited simulation from a saturated state with a more realistic heat conductivity of $\chi_{\parallel 0} = 140$ and $\gamma_e = 1.0$. The obtained profiles and pressure fluctuation level are shown in fig. 16. While the increased heat conductivity does not alter the density profile significantly it steepens the temperature

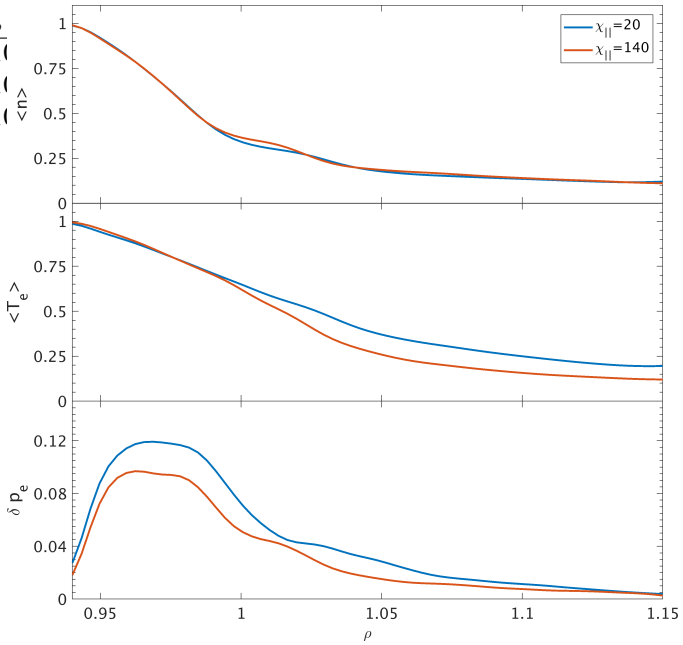

Figure 16: Impact of heat conductivity on density (top) temperature profile (center) and pressure fluctuation level (bottom) at outboard midplane position.

profile in the SOL. The fluctuation level reduces slightly which is consistent with [42], where a similar study was carried out.

5. Conclusions and Outlook

By incorporating full parametric dependencies and relaxing the Boussinesq approximation, GRILLIX was extended to a global fluid turbulence code for the tokamak edge and SOL, i.e. no assumption about fluctuation amplitudes of density or temperature is made. Further new features are electromagnetic and electron-thermal dynamics, and the implementation of the extended model was verified by analytical means and the Method of Manufactured Solutions (MMS). The flux-coordinate independent approach (FCI) is employed in GRILLIX in order to deal with realistic geometries avoiding coordinate singularities at the X-point or separatrix. As boundary contours do in general not conform with the computational grid nor the magnetic field as exceptional direction, a penalisation technique is used in order to treat sheath boundary conditions.

Turbulence simulations in circular geometry with toroidal limiter and in realistic diverted geometry at otherwise comparable parameters were presented, where parameters were chosen being characteristic for the COMPASS tokamak. A relative fluctuation level of around 30 – 40% in the SOL, with isolated highly intermittent phenomena of up to 200% fluctuation level were observed in circular geometry, which implies that a global description for SOL turbulence is indeed necessary. In diverted geometry the turbulence was found to be generally more quiescent and exhibit a stronger poloidal asymmetry. We attribute this poloidal asymmetry to local magnetic shear, which is fundamentally different in the edge region between circular and diverted geometry. Approaching regions of strong local magnetic shear turbulent structures become distorted towards the

high field side and subsequently subject to enhanced perpendicular dissipation. As this mechanism is very strong near the X-point, it tends to disconnect low field side and high field side, where curvature is favourable [19]. Due to the FCI approach GRILLIX is able to resolve the X-point region very well in contrast to field or flux-aligned approaches. However, concerning the appearance of a Quiescent X-point Region (QXR), which was found recently in MAST experiments [45], our simulation results are yet ambiguous and further investigation is required. Finally, a convergence analysis with respect to resolution was performed successfully and the impact of the heat conductivity, which was reduced for numerical reasons, was also studied.

The presented study has to be considered qualitative as there are yet important effects in the physical modeling missing, e.g. ion thermal dynamics, interaction with neutrals and more realistic sheath boundary conditions that could also take into account glancing angles of incidence. Moreover, also the core boundary condition has to be improved in order to allow for self-consistent evolution of the radial electric field in the closed field line region. Efforts to extend GRILLIX in these directions are currently ongoing. Moreover, there are also numerical constraints in order to achieve realistic parameter regimes concerning computational efficiency. The strongest time-step limitation arises from the parallel non-linear heat conduction scaling strongly with $\chi_\parallel \propto T_e^{5/2}$, for which an implicit treatment is currently pursued.

In the near future our studies would concentrate on investigation of advanced divertor concepts such as double-null, snowflake or super-X configurations, whose treatment is straight forward with GRILLIX as its numerics is independent of flux surfaces.

6. Acknowledgments

The authors would like to thank A. Bottino for computational support. This work has been carried out within the framework of the EUROfusion Consortium and has received funding from the Euratom research and training program 2014-2018 and 2019-2020 under grant agreement No 633053. The views and opinions expressed herein do not necessarily reflect those of the European Commission.

[1] T. Eich, A. W. Leonard, R. A. Pitts, W. Fundamenski, R. J. Goldston, T. Gray, A. Herrmann, A. Kirk, A. Kallenbach, O. Kardaun, A. S. Kukushkin, B. LaBombard, R. Maingi, M. A. Makowski, A. Scarabosio, B. Sieglin, J. Terry, A. Thornton, A. U. Team, J. E. Contributors, Nucl. Fusion 53 (2013) 093031.

[2] F. Halpern, P. Ricci, B. Labit, I. Furno, S. Jolliet, J. Loizu, A. Mosetto, G. Arnoux, J. Gunn, J. Horacek, M. Kočan, B. LaBombard, C. Silva, J.-E. Contributors, Nucl. Fusion 53 (2013) 122001.

[3] S. Wiesen, D. Reiter, V. Kotov, M. Baelmans, W. Dekeyser, A. Kukushkin, S. Lisgo, R. Pitts, V. Rozhansky, G. Saibene, I. Veselova, S. Voskoboynikov, J. Nucl. Mater. 463 (2015) 480.

[4] S. I. Braginskii, Transport processes in a plasma, in: A. M. A. Leontovich (Ed.), Reviews of Plasma Physics, Vol. 1, Consultants Bureau, 1965.

[5] P. Ricci, F. D. Halpern, S. Jolliet, J. Loizu, A. Mosetto, A. Fasoli, I. Furno, C. Theiler, Plasma Phys. Contr. F. 54 (2012) 124047.

[6] F. D. Halpern, P. Ricci, S. Jolliet, J. Loizu, J. Morales, A. Mosetto, F. Musil, F. Riva, T. M. Tran, C. Wersal, J. Comput. Phys. 315 (2016) 388.

[7] B. D. Dudson, J. Leddy, Plasma Phys. Contr. F. 59 (2017) 054010.

[8] P. Tamain, H. Bufferand, G. Ciraolo, C. Colin, D. Galassi, P. Ghendrih, F. Schwander, E. Serre, J. Comput. Phys. 321 (2016) 606.

[9] B. Zhu, M. Francisquez, B. N. Rogers, Comput. Phys. Commun. 232 (2018) 46.

[10] A. Stegmeir, D. Coster, A. Ross, O. Maj, K. Lackner, E. Poli, Plasma Phys. Contr. F. 60 (2018) 035005.

[11] F. Hariri, M. Ottaviani, Comput. Phys. Commun. 184 (2013) 2419.

[12] A. Stegmeir, D. Coster, O. Maj, K. Hallatschek, K. Lackner, Comput. Phys. Commun. 198 (2016) 139.

[13] A. Stegmeir, O. Maj, D. Coster, K. Lackner, M. Held, M. Wiesenberger, Comput. Phys. Commun. 213 (2017) 111.

[14] A. J. Wootton, B. A. Carreras, H. Matsumoto, K. McGuire, W. A. Peebles, C. P. Ritz, P. W. Terry, S. J. Zweben, Phys. Fluids. B 2 (1990) 2879.

[15] P. Paruta, P. Ricci, F. Riva, C. Wersal, C. Beadle, B. Frei, Phys. Plasmas 25 (2018) 112301.

[16] A. Ross, Extension of grillix: Towards a global fluid turbulence code for realistic magnetic geometries, Ph.D. thesis, Technichal University of Munich (2018).

[17] A. Ross, A. Stegmeir, P. Manz, D. Coster, W. Zholobenko, Towards global electromagnetic turbulence simulations with grillix: Relaxation of the boussinesq approximation, in preparation.

[18] R. Pánek, J. Adámek, M. Aftanas, P. Bílková, P. Böhm, F. Brochard, P. Cahyna, J. Cavalier, R. Dejarnac, M. Dimitrova1, O. Grover, J. Harrison, P. Háček, J. Havlíček, A. Havránek, J. Horáček, M. Hron, M. Imríšek, F. Janky, A. Kirk, M. Komm, K. Kovařík, J. Krbec, L. Kripner, T. Markovič, K. Mitošinková, J. Mlynář, D. Naydenkova, M. Peterka, J. Seidl, J. Stöckel, E. Štefániková, M. Tomeš, J. Urban, P. Vondráček, M. Varavin, J. Varju, V. Weinzettl, J. Zajac, the COMPASS team, Plasma Phys. Contr. F. 58 (2015) 014015.

[19] D. Farina, R. Pozzoli, D. D. Ryutov, Nucl. Fusion 33 (1993) 1315.

[20] A. Zeiler, J. F. Drake, B. Rogers, Phys. Plasmas 4 (1997) 2134.

[21] M. Francisquez, Global braginskii modeling of magnetically confined boundary plasmas, Ph.D. thesis, Dartmouth College, Hanover (New Hampshire) (2018).

[22] K. Salari, P. Knupp, Code verification by the method of manufactured solutions, Sandia National Laboratories, Sandia Report SAND2000-1444 (2000).

[23] A. Ross, A. Stegmeir, D. Coster, Contrib. Plasm. Phys. 58 (2018) 478.

[24] J. Loizu, P. Ricci, F. D. Halpern, S. Jolliet, Phys. Plasmas 19 (2012) 122307.

[25] P. C. Stangeby, The Plasma Boundary of Magnetic Fusion Devices, Plasma Physics Series, Institute of Physics Publishing, 2000.

[26] U. Stroth, P. Manz, M. Ramisch, Plasma Phys. Contr. F. 53 (2011) 024006.

[27] E. Viezzer, T. Pütterich, G. Conway, R. Dux, T. Happel, J. Fuchs, R. McDermott, F. Ryter, B. Sieglin, W. Suttrop, M. Willensdorfer, E. Wolfrum, the ASDEX Upgrade Team, Nucl. Fusion 53 (2013) 053005.

[28] A. Arakawa, J. Comput. Phys. 135 (1997) 103.

[29] E. Hairer, S. P. Norsett, G. Wanner, Solving ordinary Differential Equations I. Nonstiff Problems, 2nd Edition, Springer Series in Computational Mathematics, Springer-Verlag, 1993.

[30] P. Hill, B. Shanahan, B. Dudson, Comput. Phys. Commun 213 (2017) 9.

[31] B. Shanahan, B. Dudson, P. Hill, Fluid simulations of plasma laments in stellarator geometries with BSTING, arXiv (2018) 1808.08899v1.

[32] M. Shashkov, S. Steinberg, J. Comput. Phys. 118 (1995) 131.

[33] M. Shashkov, Conservative Finite-Difference Methods on General Grids, CRC Press, 1996.

[34] L. Isoardi, G. Chiavassa, G. Ciraolo, P. Haldenwang, E. Serre, P. Ghendrih, Y. Sarazin, F. Schwander, P. Tamain, J. Comput. Phys. 229 (2010) 2220.

[35] H. Bufferand, B. Bensiali, J. Bucalossi, G. Ciraolo, P. Genesio, P. Ghendrih, Y. Marandet, A. Paredes, F. Schwander, E. Serre, P. Tamain, J. Nucl. Mater. 438 (2013) S445.

[36] G. E. Karniadakis, M. Israeli, S. A. Orszag, J. Comput. Phys. 97 (1991) 414.

[37] W. Hackbusch, Multi-Grid Methods and Applications, Springer-Verlag, 1985.

[38] B. Scott, Low frequency fluid drift turbulence in magnetised plasmas, Habilitation thesis, Heinrich-Heine University Düsseldorf (2000).

[39] A. J. Cerfon, J. P. Freidberg, Phys. Plasmas 17 (2010) 032502.

[40] M. Held, M. Wiesenberger, A. Stegmeir, Comput. Phys. Commun. 199 (2016) 29.
[41] F. D. Halpern, S. Jolliet, J. Loizu, A. Mosetto, P. Ricci, Phys. Plasmas 20 (2013) 052306.
[42] B. Zhu, M. Francisquez, B. N. Rogers, Phys. Plasmas 24 (2017) 055903.
[43] P. Manz, A. Stegmeir, B. Schmid, T. T. Ribeiro, G. Birkenmeier, N. Fedorczak, S. Garland, K. Hallatschek, M. Ramisch, B. D. Scott, Phys. Plasmas 25 (2018) 072508.
[44] J. R. Myra, D. A. D'Ippolito, X. Q. Xu, R. H. Cohen, Phys. Plasmas 7 (2000) 2290.
[45] N. R. Walkden, J. Harrison, S. A. Silburn, T. Farley, S. S. Henderson, A. Kirk, A. Thornton, T. M. Team, Nucl. Fusion. 57 (2017) 126028.